-- Compressed PDF version --

Research Article Vol. 33, No. 2 / 27 Jan 2025 / Optics Express 3562
Optics EXPRESS

Efficient X-ray dark field contrast simulations using a condensed history approach

NICHOLAS FRANCKEN,* JONATHAN SANCTORUM, BEN HUYGE, JAN SIJBERS, AND JAN DE BEENHOUWER

imec-Vision Lab, Department of Physics, University of Antwerp, Universiteitsplein 1, Antwerp, B- 2610, Belgium
nicholas.francken@uantwerpen.be

Abstract: Due to the growing interest in X-ray phase contrast imaging (XPCI), the development of XPCI simulators has become an active field of research. Efficient computer simulations are a prime tool for optimizing the XPCI setup and acquisition process. In addition to phase contrast, modern XPCI setups provide insight into the unresolvable sample micro structure distribution through the dark field signal. However, to accurately simulate XPCI dark field signals, the virtual sample model should contain many fine structures, considerably increasing the simulation time. Moreover, accurately modeling micro structure distributions is challenging and the micro structure distribution of one virtual sample cannot be easily transferred to another. In this work, we apply a condensed history approach to dark field simulations, removing the need to explicitly model the micro structures in the virtual sample. Instead, a tunable dark field material parameter, representing a measure of the material micro structure distribution, is attached to the sample. The condensed history simulation model offers a substantial increase in simulation speed and the dark field material parameter is easily transferable between samples. The implementation is validated using the edge illumination XPCI setup. Condensed history simulations are compared to real data, showing good agreement, and the simulation speed increase is presented for increasing sample thickness and field of view. The simulation model is shown to remain valid even for thick samples. Simulated computed tomography data sets, with and without explicit micro structure, are favorably compared to each other.

© 2025 Optica Publishing Group under the terms of the Optica Open Access Publishing Agreement

1. Introduction

The dark field signal measured in many X-ray phase contrast imaging (XPCI) setups allows probing the micro structure distribution of an object, supplying information on the presence of structures with a length scale below the spatial resolution of the setup. The dark field, often interpreted as ultra-small angle X-ray scattering (USAXS), thereby provides complementary information next to the attenuation and refraction (i.e. differential phase) signals. Many application areas for X-ray dark field imaging have been identified, ranging from chest imaging [1–3] to threat detection [4,5], and from inspection of composite materials [6,7] to inspection of foods [8]. A crucial component in the ongoing research and optimization process of XPCI, including dark field imaging, is the availability of performant simulation software. For example, in [9] a study was performed comparing available simulators for speckle-based imaging [10]. In general, XPCI simulations require a complex wave optics model (e.g. [11–13]), but depending on the XPCI setup and acquisition geometry, the much simpler ray optics description can be used [14,15]. If wave properties, such as interference, cannot be neglected, but one still wants to leverage the simplicity of ray optics, a combination of the two methods can be applied [16]. Alternatively, post-processing techniques can be applied in tandem with a ray optics model to simulate XPCI setups that cannot be fully described with ray optics, such as grating interferometry [17]. In this work, the edge illumination (EI) XPCI setup will be considered [18], for which the validity limits of a ray optics approach have been previously investigated [19].

#544864 https://doi.org/10.1364/OE.544864
Journal © 2025 Received 15 Oct 2024; revised 29 Nov 2024; accepted 2 Dec 2024; published 24 Jan 2025

-- Compressed PDF version --

Optics EXPRESS

Several ray optics based X-ray simulation tools have been developed (or extended) to perform XPCI, which requires the inclusion of X-ray refraction in the simulation model [20–23]. In all these tools, dark field signal is generated by many refraction events happening at a scale below the detector spatial resolution. Hence, to generate dark field signal, the virtual sample used for an XPCI simulation has to contain a high number of fine micro structures. This inevitably slows down the simulation, as the rays (or photons, depending on the simulation tool) have to be traced across more material interfaces. Moreover, the shape and size distribution of these micro structures will determine the measured strength of the dark field signal, but often these distributions are unknown and/or difficult to calculate. Even when known, translating these distributions to a virtual sample model is not a straightforward task and can easily lead to e.g. unworkable large file sizes or overlapping structures (resulting in badly defined ray tracing). In addition, the modeling process of the micro structure has to be repeated for each new sample.

One way to alleviate these problems is by using a condensed history approach for simulating the dark field signal [24,25]. In the general case, during a condensed history simulation, ray events are ignored and instead added to the ray *history* until at some predetermined threshold the entire ray history is *condensed* into a single ray update event. As the condensed history approach allows aggregating many consecutive events into a single event, it is particularly applicable to dark field simulations, where many interactions (i.e. refraction/reflection) happen at a very small scale. Instead of having to explicitly add the micro structures to the virtual sample, within this condensed history approach only the bounding surfaces of regions containing micro structures have to be provided, together with some material parameter dictating the scatter magnitude of the condensed history dark field update. This dark field parameter can be calibrated based on dark field data from either real acquisitions or simulations using explicit micro structures. Condensed history approaches typically have a limit on the ray propagation distance, above which the model no longer gives accurate results. This model validity limit has not yet been tested for the case of condensed history dark field updates.

Characterization of the dark field strength by some coefficient has been explored in previous work on other XPCI methods [26,27]. The dark field material parameter that we introduce for calibrating the condensed history dark field update is analogous to the linear diffusion coefficient that has been introduced for grating interferometry in [27]. A subtle difference is that the linear diffusion coefficient was established to quantify dark field in already acquired data, while our proposed dark field material parameter is part of the forward simulation model used to generate data. In this sense, our method is a reverse approach compared to that in [27].

In this work, a dark field material parameter is added to the recently developed CAD-ASTRA toolbox [20,28], allowing a condensed history approach for XPCI dark field simulations. This work extends the preliminary results presented in [29], where simulated radiographs using a condensed history dark field approach were compared to simulations using explicit micro structure. We expand on those results by calibrating the dark field parameter using real data, performing experiments to test the increased simulation speed and model validity limit, and comparing reconstructions from simulated computed tomography (CT) data sets with and without the condensed history approach.

2. Methods

2.1. Edge illumination

The edge illumination XPCI setup makes use of two absorbing masks with slit-shaped apertures. One is placed in front of the sample (sample mask) and splits the X-ray beam into smaller beamlets. The other is placed in front of the detector (detector mask) and creates insensitive regions on the detector pixels. For both masks, the aperture period is the (demagnified) pixel size or a whole multiple thereof (the latter being referred to as column-skipping masks). Due to

-- Compressed PDF version --

Optics EXPRESS

the slit shape of the mask apertures, the EI setup is sensitive only to refraction in the direction perpendicular to the slit direction (e.g. horizontal refraction in the case of vertical slits).

During an EI acquisition, the sample mask is stepped lateral to the aperture orientation and projections are recorded at several sample mask positions. Combining the different mask step projections results in an intensity profile that can be modeled as a sum of Gaussian functions for each detector pixel, referred to as the illumination curve (IC) [30,31]. This model can be further simplified by taking only a single Gaussian in the sum:

$$IC(x) = A \exp\left(\frac{-(x-\mu)^2}{2\sigma^2}\right) + b \quad . \tag{1}$$

The transmission, refraction and dark field contrasts are extracted by comparing the IC fit parameters of an EI acquisition to the reference IC parameters of a flat field EI acquisition. The transmission, T, is defined as the ratio between the areas under the IC curves, the refraction, θ, is the angular beamlet deviation, measured through the shift in the IC peak location, and the dark field, σ^2_{DF}, is the angular beamlet broadening, measured as a broadening of the IC curve.

$$T = \frac{A_s \sigma_s}{A_f \sigma_f} \quad , \tag{2}$$

$$\theta = \frac{M}{z_{od}}(\mu_s - \mu_f) \quad , \tag{3}$$

$$\sigma^2_{DF} = \left(\frac{M}{z_{od}}\right)^2 (\sigma_s^2 - \sigma_f^2) \quad , \tag{4}$$

where A, μ and σ indicate the IC amplitude, peak position and standard deviation, respectively. The s and f subscripts refer to either sample or flatfield acquisition, M is the geometric cone-beam magnification, and z_{od} is the object-detector distance.

2.2. CAD-ASTRA

As EI is a non-interferometric XPCI technique, the ray tracing CAD-ASTRA simulation toolkit can be used to accurately model the setup [19,20,32]. The physics model of CAD-ASTRA contains the Beer-Lambert law to model ray attenuation and Snell's law to model ray refraction or reflection. At each interface, the ray intensity and direction is updated based on the distance travelled through the current medium, the incident angle on the interface, and the material parameters defined during the simulation setup. While the transmission and refraction contrasts follow straightforwardly from the Beer-Lambert law and Snell's law, respectively, the dark field contrast is generated by rays undergoing many refraction events at a scale below the system spatial resolution.

A CAD-ASTRA simulation setup is a collection of surface meshes, which are each given an attenuation coefficient, refractive index and surface roughness parameter (to compensate for the perfectly smooth edges of surface meshes). The EI masks, for example, are two collections of bars, which are given a high attenuation coefficient as to be completely absorbing. For samples consisting of multiple materials, such as e.g. a powder within a container, nested surface meshes with different material properties can be defined.

2.3. Condensed history dark field

In the above example of a powder, each grain has to be modeled individually (e.g. as a spherical surface mesh with certain material properties). Next, all grains have to be nested inside a larger mesh representing the container. A realistic distribution of the grains requires detailed knowledge of the powder sample in question, which is often not available. Moreover, the large increase in

-- Compressed PDF version --

Optics EXPRESS

the number of meshes required to generate a measurable dark field signal (easily in the range of tens of thousands) causes a considerable simulation performance decrease, as for each ray Snell's law has to be calculated at each mesh interface.

These problems of mesh distribution and simulation performance decrease, illustrated using powders as example, are present for all samples containing micro structures, i.e. for all dark field related experiments. One solution is to bundle all the meshes that characterize a micro structure into a single mesh and condense all the refraction events into a single ray update. The condensed update will depend on the distance the ray travelled through the mesh representing a micro structure region and a new dark field material parameter that depends on the specifics of the micro structure (number density, individual structure size, etc.).

More specifically, the condensed history ray update aims to model the beamlet broadening that is normally induced by the many ray refraction events that happen when traversing the micro structures. To this end, a surface mesh is defined that serves as a bounding region within which a micro structure distribution is present, instead of generating all the micro structures explicitly as individual meshes. The mesh is given a dark field material parameter p_{DF} that depends on the micro structure in question. As it represents angular broadening per distance unit, p_{DF} has units of $\mathrm{rad}^2\,\mathrm{mm}^{-1}$, with mm the arbitrary distance unit used in this work. During simulation, rays traverse the mesh without undergoing direction changes due to micro structures. However, when they exit the mesh, a cumulative ray direction update is applied, as presented in Fig. 1. First, the angular broadening of the rays is defined as a scaled Gaussian distribution, centered around zero: $\mathcal{N}(0, \alpha_{\mathrm{DF}}^2)$. The standard deviation α_{DF} used to scale the distribution is defined as $\alpha_{\mathrm{DF}} = \sqrt{p_{\mathrm{DF}}\,\Delta l}$, with Δl the ray path length through the mesh. To convert the angular broadening to a length measure, the sine is taken, resulting in the "length scaling" distribution $\mathcal{N}(0, \sin^2(\alpha_{\mathrm{DF}}))$. Then, two orthogonal unit vectors, $\mathbf{u}_1$ and $\mathbf{u}_2$, are defined in the plane perpendicular to the ray direction $\mathbf{R}_{\mathrm{old}}$. Each of these two vectors $\mathbf{u}_i$ is scaled with a different sample s_i from the length scaling Gaussian distribution, resulting in the dark field update vectors $\mathbf{v}_{1,2}$:

$$s_{1,2} \sim \mathcal{N}(0, \sin^2(\alpha_{\mathrm{DF}})) \quad , \tag{5}$$

$$\mathbf{v}_1 = s_1\,\mathbf{u}_1 \quad , \tag{6}$$

$$\mathbf{v}_2 = s_2\,\mathbf{u}_2 \quad . \tag{7}$$

Finally, both scaled vectors $\mathbf{v}_{1,2}$ are added to the current ray direction $\mathbf{R}_{\mathrm{old}}$ to determine the updated ray direction:

$$\mathbf{R}_{\mathrm{new}} = \mathbf{R}_{\mathrm{old}} + \mathbf{v}_1 + \mathbf{v}_2 \quad . \tag{8}$$

Using this approach, only a single mesh is required to model a micro structure region and only a single ray update is required to model dark field effects.

Condensed history models usually have a validity limit in the form of a maximal ray depth (or mesh thickness) for which a condensed history update still gives accurate results. This is because the condensed history update is typically an approximation of the actual summed individual updates. Should the simulated mesh be thicker than the validity limit, it can be split into multiple thinner slices.

2.4. Dark field parameter calibration

The dark field parameter can be calibrated through either simulated or real data. When calibrating using simulated data, two virtual wedge meshes are generated. One wedge is filled with micro structures, e.g. tightly packed thin cylinders, while the other remains a solid wedge, as in [29]. A simulation using only the explicit micro structure wedge, which is given a refractive index based on the expected material, gives a reference dark field image. Then, a simulation using only the solid wedge is performed, where an initial guess for the dark field parameter is given to the solid

-- Compressed PDF version --

Optics EXPRESS

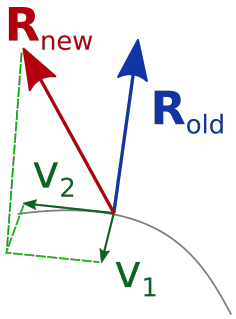

Fig. 1. Sketch of the condensed history ray direction update performed when a ray leaves a dark field mesh. $\mathbf{R}_{\text{old}}$ and $\mathbf{R}_{\text{new}}$ are the original and updated ray directions, respectively, and $\mathbf{v}_1$ and $\mathbf{v}_2$ are the orthogonal unit vectors $\mathbf{u}_1$ and $\mathbf{u}_2$, scaled with the random samples s_1 and s_2, respectively.

wedge. The resulting dark field image is compared to the reference dark field from the explicit micro structure simulation by using the root mean squared error (RMSE) as metric. In an iterative manner, the dark field parameter is updated to minimize the RMSE between the reference and condensed history dark field signals. When calibrating using real data, an analogous approach is followed, but now the reference dark field image is not constructed from a simulation, but from a real data acquisition. An EI acquisition is performed of a 3D printed hollow wedge sample, filled with a micro structure material (e.g. a powder). Then, as before, simulations are run for a virtual solid wedge, but now making sure it has the same dimensions as the physical wedge. The solid wedge is again given an initial guess for the dark field parameter, which is iteratively optimized using a RMSE minimization. Once this calibration is done, through either simulated or real data, the retrieved dark field parameter can be used in any future simulations of the same micro structure/material, removing the need of explicit micro structure modeling. It is relevant to note that the calibration meshes are typically relatively small (in the order of one or a couple cm). It is thus possible, for example, to calibrate the dark field parameter on such a small wedge containing explicit micro structures, and then use it to simulate large micro structure samples, for which an explicit micro structure representation is prohibited due to excessive file sizes.

3. Experiments

All experiments were performed using simulated EI data generated with the CAD-ASTRA toolbox [20,32]. The setup parameters that were experiment specific are all given in their respective subsection, while the values that were kept constant are given here. Each mesh was given a linear attenuation coefficient μ_{lin}, refractive index decrement δ, and dark field parameter p_{DF}. For the condensed history dark field simulations, no refraction was considered (i.e. $\delta = 0$), as we were only interested in generating dark field signal. The simulated EI masks were made out of gold, had a thickness of 225 µm, and had a projected aperture width (at the detector plane) of 30 µm. The pixel size for all experiments was 150×150 µm^2 and all meshes were given a surface roughness parameter of 0.001 (based on [32]). Furthermore, all distances were expressed in millimeters, hence the values of the dark field material parameter were determined relative to this distance unit.

3.1. Calibration on real data

For this first experiment, real data was acquired using the EI setup in the FleXCT system at the University of Antwerp [33,34]. The setup had a SOD (source-object distance) and SDD (source-detector distance) of 890 mm and 1260 mm, respectively. The sample was a hollow wedge,

-- Compressed PDF version --

Optics EXPRESS

3D printed using a polylactic acid (PLA) filament, with one right angle and with dimensions of 1.5 cm (length) × 1.5 cm (width) × 2 cm (height) (see Fig. 2). The wedge was first filled with spelt flour and then with cardamom, which was expected to have larger grain sizes than the flour. Both scans consisted of 21 mask steps, each separated by 5 µm. The source was set to 45 kVp and 60 W, and for every image three averages were taken, each with an exposure time of 2.5 s. For the CAD-ASTRA simulation, a copy of the FleXCT geometry was used. For the virtual sample, first a solid wedge mesh was created with the same measures as the printed wedge, representing the outer surface of the sample. Then, a slightly smaller wedge was placed inside the outer surface wedge, representing the powder-filled region of the hollow real-world wedge. Finally, the mesh representing the powder-filled region was given a non-zero dark field parameter that was optimized in an iterative manner, as described in section 2.4. Refraction of the wedge meshes was set to zero, as it does not contribute to the dark field signal in the bulk material. The linear attenuation coefficients of the outer and inner wedge were calibrated in the same manner as the dark field parameter.

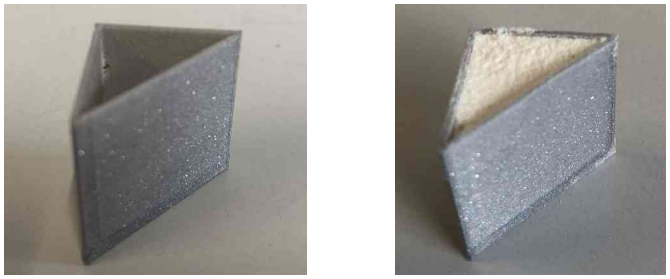

Fig. 2. The hollow 3D printed wedge, empty (left) and filled with flour (right).

To validate the calibrated dark field parameters, a more complex sample was designed and 3D printed (see Fig. 3). The outer dimensions of the sample were 6 cm (length) × 1.2 cm (width) × 1 cm (height). The holes in the sample were filled with spelt flour and a FleXCT acquisition was performed, using the same acquisition parameters as for the wedge scans. The retrieved FleXCT dark field signal was compared with that of a CAD-ASTRA simulation in which the calibrated dark field parameter of spelt flour was used. The sample used for the CAD-ASTRA simulation was the inverse of the printed sample, i.e. it contained meshes with the shapes of the holes in the printed sample, as these are the micro structure regions.

Fig. 3. A render of the more complex sample (left) and the 3D printed version, filled with flour (right).

3.2. Performance comparison

To evaluate the CAD-ASTRA performance difference between explicit micro structure meshes and solid meshes with a dark field parameter, two experiments were performed. One compared performance based on mesh thickness and the other based on field of view (i.e. detector size). The simulations were performed on a desktop computer equipped with an Intel Core i7-5960X

-- Compressed PDF version --

Optics EXPRESS

CPU and NVIDIA GeForce RTX 3070 GPU. First, slab meshes with different thicknesses were created. An example is presented in Fig. 4. The width and height of the slabs was kept constant at 15 mm and 1.5 mm, respectively, and the micro structure meshes consisted of cylinders with a diameter of 20 µm. The cylinders were placed parallel to each other in the micro structure meshes using Poisson disk sampling and were given a minimum separation distance of 2 µm to avoid overlapping structures. The depth of the slabs was varied between 1 and 10 mm. Each simulation consisted of 21 equidistant mask steps in the [−50 µm, 50 µm] interval and had a detector size of 256×11 pixels. The micro structure slabs had $\delta = 3 \times 10^{-7}$ and $p_{\mathrm{DF}} = 0\,\mathrm{rad}^2\,\mathrm{mm}^{-1}$, while the solid slabs had $\delta = 0$ and $p_{\mathrm{DF}} = 5{\times}10^{-11}\,\mathrm{rad}^2\,\mathrm{mm}^{-1}$, and both types of slabs had $\mu_{\mathrm{lin}} = 0.03\,\mathrm{mm}^{-1}$.

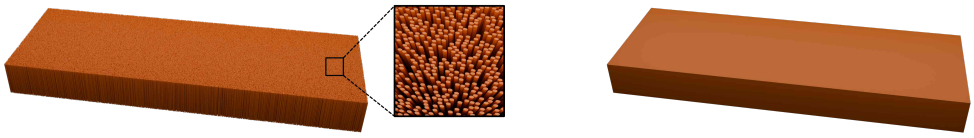

Fig. 4. Render of an example micro structure (left) and solid (right) slab used for the performance comparison experiment.

For the field of view (FOV) experiment, the explicit micro structure and solid slabs with a 5 mm thickness from the previous experiment were used. Their height was scaled to 30 mm. All experimental and material parameters were kept identical to the previous experiment, except the detector size. For this experiment, a square detector was defined, the size of which was varied from 10 × 10 to 100 × 100 pixels. For each detector size, the slabs covered the entire FOV.

3.3. Validity limit

To test the mesh thickness limit for our condensed history implementation, two simulations were performed. First, a solid wedge mesh was created with dimensions of 39.6 × 19.8 × 30.8 mm (see the yellow mesh in Fig. 5). The mesh was given a linear attenuation coefficient $\mu_{\mathrm{lin}} = 0.02\,\mathrm{mm}^{-1}$ and dark field parameter $\sigma_{\mathrm{DF}} = 1.3{\times}10^{-10}\,\mathrm{rad}^2\,\mathrm{mm}^{-1}$, no refraction was included. In this case, a single dark field update was applied to each ray traversing the wedge mesh.

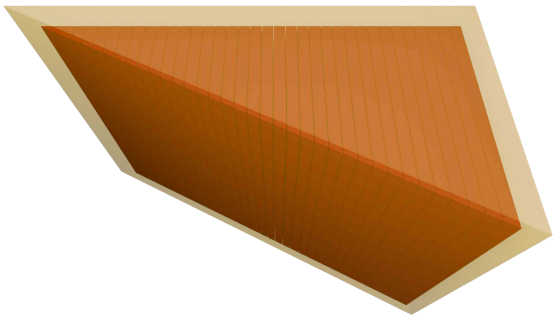

Fig. 5. Render of a sliced wedge (red), nested inside a solid wedge (yellow), used to determine the mesh thickness validity limit for the condensed history approach.

Second, a sliced wedge mesh was created with dimensions of 36 × 18 × 28 mm (see the red mesh in Fig. 5). Each slice was 0.95 mm thick and spaced 0.05 mm from the next slice. The same material parameters were given to the sliced wedge mesh as to the solid wedge and the sliced wedge was nested in the solid wedge (as in Fig. 5). In this case, a dark field update was again applied to each ray whenever it exited the solid wedge, but now as well when it exited one of the

-- Compressed PDF version --

Optics EXPRESS

nested slices. In effect, this shortens the ray propagation distances before a dark field update is applied, without changing the shape or size of the object being imaged.

3.4. CT reconstruction

Two simulated EI-CT data sets were generated, one with three cylindrical patches containing different micro structures, and one with three solid cylinders which were given a dark field material parameter. A color-coded render of both the samples is given in Fig. 6. For the micro structure sample, the red, green and blue patches contained cylinders with a diameter of 10 µm, 30 µm and 50 µm, respectively. All cylinders were given an attenuation of $\mu_{\text{lin}} = 0.04\,\text{mm}^{-1}$, and the red, green and blue micro structures had $\delta = 3 \times 10^{-7}$, $\delta = 2 \times 10^{-7}$ and $\delta = 5 \times 10^{-7}$, respectively. Wedges with the same micro structures and refractive indices were generated to calibrate the dark field parameter for the solid cylinder meshes in the manner outlined above. The CT simulations consisted of 360 projection angles in the [0°, 360°) rotation interval, with 15 equidistant mask steps in the [−50 µm, 50 µm] interval for each projection angle. The detector had 256×11 pixels, out of which the central slice was reconstructed with the ASTRA toolbox [28]. For each of the three micro structure patches, the fill-factor was calculated (the fraction of the total cylindrical volume occupied by the micro structure meshes). These fill-factors were used as a scaling factor for the attenuation in the dark field parameter simulation, which is otherwise overestimated [29].

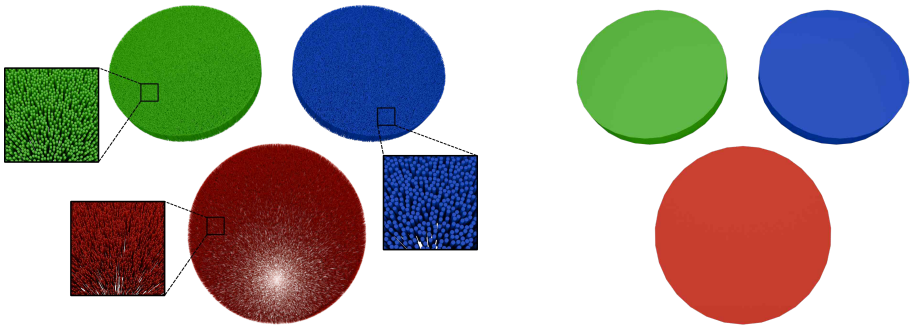

Fig. 6. Render of the micro structure (left) and solid (right) CT experiment samples.

4. Results

4.1. Calibration on real data

The linear attenuation coefficients found for the outer and inner wedge were $0.7\,\text{cm}^{-1}$ and $0.3\,\text{cm}^{-1}$, respectively. Dark field signal results for the different powders are presented in Fig. 7. The CAD-ASTRA simulations, based on a single fitted dark field parameter for each of the two powders, narrowly follow the dark field signal obtained from the FleXCT acquisitions. At the thick edge of the wedge, there are some noticeable dark field peaks for the FleXCT data, which are absent for the CAD-ASTRA data. The calibration method, detailed in section 2.4, required 21 iterations (average of 10.22 s per iteration) for the spelt flour and 25 iterations (average of 10.15 s per iteration) for the cardamom. The dark field parameters were $6.96{\times}10^{-11}\,\text{rad}^2\,\text{mm}^{-1}$ for the spelt flour and $4.14{\times}10^{-11}\,\text{rad}^2\,\text{mm}^{-1}$ for the cardamom. In Fig. 8, an example flatfield IC and sample IC (of the spelt flour wedge) are shown for both the FleXCT acquisition and CAD-ASTRA simulation. The IC offset in the FleXCT data is clearly visible, compared to the completely absorbing masks used in CAD-ASTRA.

The comparison between FleXCT data of the sample in Fig. 3, where the holes were filled with spelt flour, and a CAD-ASTRA simulation using the spelt flour dark field parameter $p_{\text{DF}} =$

-- Compressed PDF version --

Optics EXPRESS

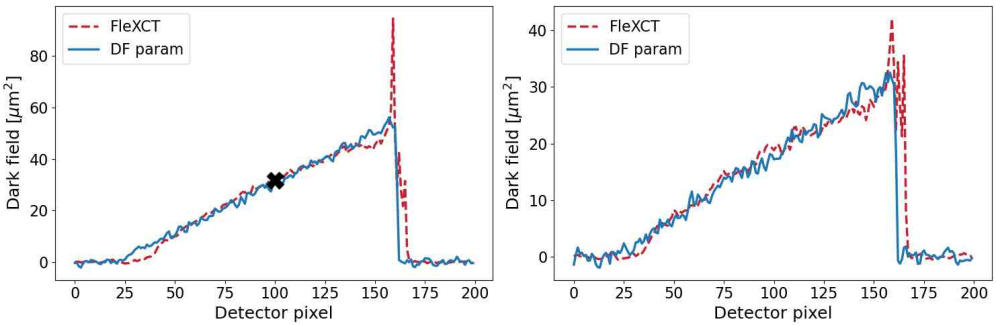

Fig. 7. Calibration of dark field parameter CAD-ASTRA simulations based on FleXCT data of spelt flour (left) and cardamom (right) using the wedge in Fig. 2. The marker in the left panel indicates the pixel for which the ICs are shown in Fig. 8.

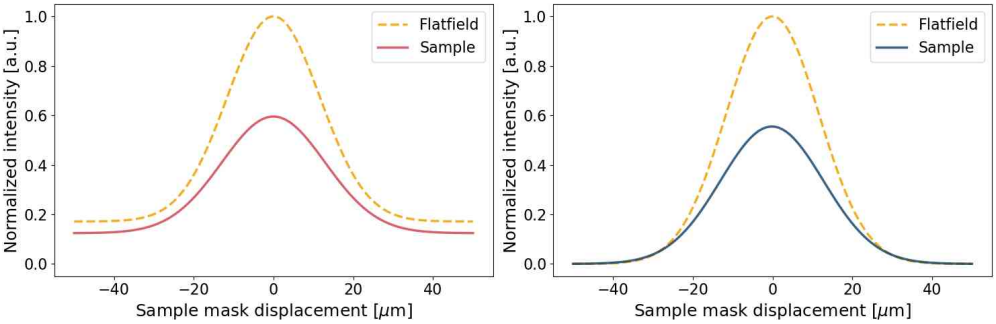

Fig. 8. The flatfield and sample ICs of the marked pixel in Fig. 7 for the FleXCT (left) and CAD-ASTRA (right) spelt flour data. Note that the dark field field was correctly simulated, even though the CAD-ASTRA simulation did not include IC offsets.

6.96×10^{-11} rad^2 mm^{-1}, is shown in Fig. 9. A good comparison is found between the two dark field signals, with the biggest differences located between consecutive dark field regions and not within the dark field regions themselves.

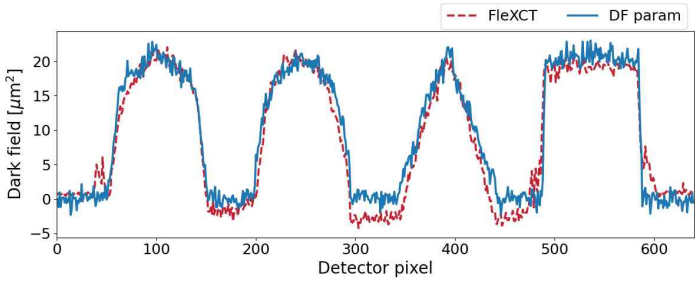

Fig. 9. Comparison between the dark field of FleXCT data using spelt flour and a CAD-ASTRA simulations using the corresponding dark field parameter, for the sample presented in Fig. 3.

4.2. Performance comparison

The results for the performance comparison are shown in Fig. 10. Apart from the micro structure and solid mesh execution times, the flat field execution times are given as a lower bound. It is

-- Compressed PDF version --

Optics EXPRESS

found that the explicit micro structure mesh execution time scales roughly linear with the mesh thickness, going from just under 20 s for a 1 mm thick slab to just under 100 s for a 10 mm thick slab. On the other hand, the dark field parameter execution time does not increase with increasing mesh thickness, has an average execution time of 10.2 s, and only adds marginally to the flat field execution time, with an average of 9.6 s. For the FOV experiment, the execution times scale roughly quadratically for all three curves, but the explicit micro structure mesh curve is much steeper. The time difference between the two simulation methods increases from roughly 3.5 s for the 10×10 detector to 243.2 s for the 100×100 detector.

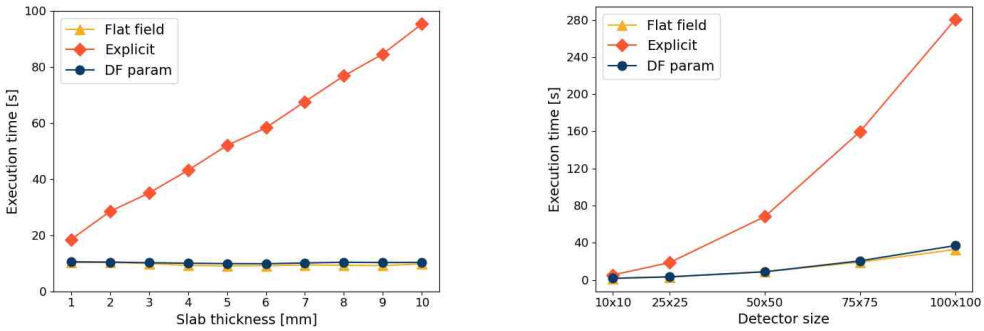

Fig. 10. Relation between mesh thickness (for slabs such as those in Fig. 4) and CAD-ASTRA execution time (left), and relation between FOV and CAD-ASTRA execution time (right). The flat field simulation, without any objects apart from the EI masks, serves as a lower limit for the execution time.

4.3. *Validity limit*

In Fig. 11, the attenuation and dark field signals are compared between simulations using only the solid wedge and both the solid and sliced wedges in Fig. 5. While the condensed history dark field update is applied multiple times for the sliced wedge simulation, the results are almost identical to a single update in the solid wedge simulation. Furthermore, the simulated ICs at high wedge thicknesses are very similar. For the thickest part of the wedge, the dark field signal starts saturating, i.e. it starts deviating from a linear slope, which is a known effect [35]. These results indicate that any potential mesh thickness validity limit lies beyond the mesh thickness limit determined by dark field saturation.

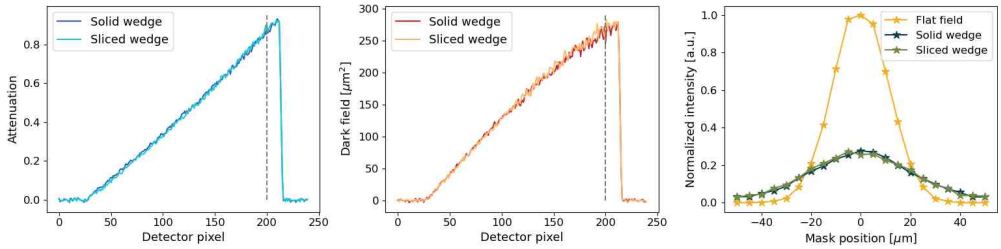

Fig. 11. Comparison of attenuation (left) and dark field (middle) signal between a solid wedge and sliced wedge. The right panel shows the ICs for the pixel indicated with a gray dashed line in the other panels.

-- Compressed PDF version --

Optics EXPRESS

4.4. CT reconstruction

The attenuation and dark field reconstructions of the EI-CT simulations are shown in Fig. 12, while in Fig. 13 the box plots are given for regions of interest (ROIs) inside the three cylinders. The three estimated dark field parameters were $p_{\mathrm{DF}} = 1.33{\times}10^{-11}$ rad^2 mm^{-1}, $p_{\mathrm{DF}} = 3.48{\times}10^{-11}$ rad^2 mm^{-1} and $p_{\mathrm{DF}} = 2.69{\times}10^{-11}$ rad^2 mm^{-1}, for the cylinder covered by ROI 1, 2 or 3, respectively. For the attenuation box plots of the dark field parameter simulation, the values inside the ROIs were scaled with the fill-factor of the corresponding micro structure mesh. The variance in the explicit micro structure simulation is noticeably higher than for the dark field parameter simulation, with even some negative attenuation and dark field values. The average within each ROI, however, shows good agreement between the two simulations, both for the (scaled) attenuation and dark field.

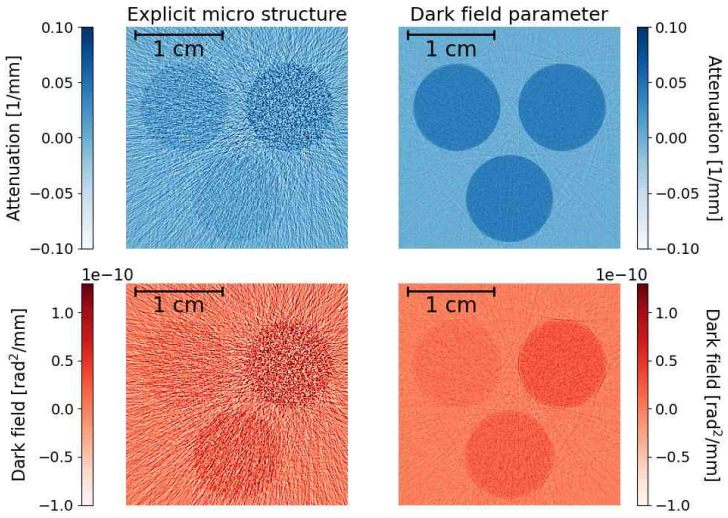

Fig. 12. Comparison between the attenuation (top) and dark field (bottom) CT reconstructions for explicit micro structures (left) and dark field parameters (right).

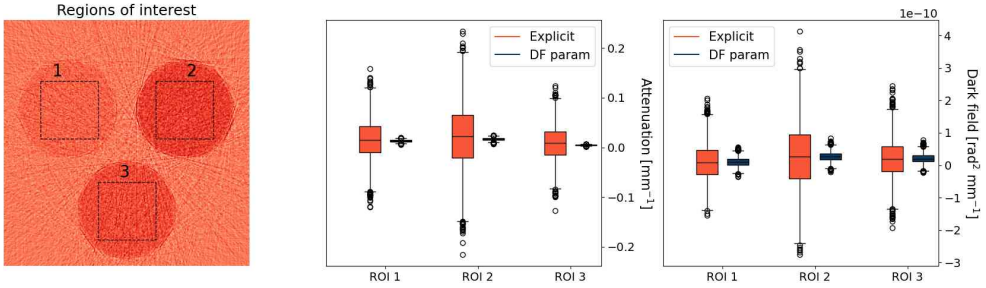

Fig. 13. Box plots of the attenuation (middle) and dark field (right) CT reconstructions for both the explicit micro structure and dark field parameter results, using the ROIs defined in the left panel.

5. Discussion

Our proposed condensed history method requires calibrating a dark field material parameter based on experimental or simulated data containing a dark field signal. Therefore, it could

-- Compressed PDF version --

Optics EXPRESS

initially seem impractical to use the dark field parameter, as it requires another data set based on real micro structures. However, often a simple calibration experiment/simulation using a small wedge sample with explicit micro structures is sufficient for many follow up simulations of more complex samples, using the dark field parameter. For example, once a relationship between micro structure size and dark field signal is established based on a sample wedge mesh containing explicit structures, extra- and interpolation of this relationship can be performed using the more efficient dark field parameter. Extrapolation using the dark field parameter for larger/thicker samples is especially useful, as an extrapolation using explicit micro structures could be prohibited due to excessive memory requirements.

The dark field signal obtained from the CAD-ASTRA simulations closely follows the dark field signal of the FleXCT acquisitions. Nonetheless, it is important to note that the FleXCT X-ray source is inherently polychromatic and the CAD-ASTRA simulation was performed using a single dark field parameter, using the concept of a single “effective energy" to approximate the polychromatic spectrum. Looking closely at the FleXCT dark field curves, however, it can be seen that they slightly deviate from a purely linear signal, which is assumed to be a beam hardening effect. This effect is not observed for the essentially monochromatic CAD-ASTRA simulations, which are completely linear. In cases where the beam hardening is more pronounced, a polychromatic simulation will have to be used to accurately model the dark field signal, analogously to sample attenuation simulations.

Dark field is known to exhibit signal at object edges, which is not related to micro structures but rather to refraction effects. This signal can be seen for the FleXCT data at the thick edge of the wedge in Fig. 7. As the CAD-ASTRA simulation did not include refraction, the edge peak is absent for the simulated dark field. For more detailed simulations, the refractive index of the material can be included for ray refraction at the outer edges of the sample, together with a dark field parameter for the bulk micro structure material. When combining refraction and condensed history dark field in a simulation, it is important to make sure one does not overestimate the dark field signal. This can be done by e.g. making sure the sample does not have large concentrations of refracting structures with dimensions below the imaging setup spatial resolution, together with a non zero dark field parameter. For the simulated dark field signal shown in Fig. 9, only the differently shaped dark field regions were included and not the PLA structure within which the holes were located. This could explain the discrepancy between the simulated and the experimentally measured dark field signal for the regions between the different holes. The negative values in the FleXCT dark field are expected to be related to polychromatic effects in the encompassing PLA structure.

The IC definition in Eq. (1) includes an offset term, which represents the fraction of X-rays that penetrate through the mask septa. In CAD-ASTRA, the masks are typically made completely absorbing, resulting in zero offset. In real acquisitions, however, there is often a non-zero offset. As illustrated in Fig. 8, it was found that the condensed history update can correctly model IC broadening, even though the FleXCT data includes a clear IC offset and the CAD-ASTRA simulation has no offset, as it used completely absorbing masks.

From the performance study, it is found that using the condensed history dark field results in substantially faster simulations compared to using explicit micro structures, both for thicker meshes and larger FOVs. An increase of almost an order of magnitude is found for a mesh thickness of 10 mm, which is expected to increase linearly for increasing mesh thickness. This becomes especially relevant in the context of CT simulations, where each projection angle benefits from this simulation speed increase. Furthermore, we see that, as the number of rays increases quadratically when the detector area increases, so does the execution time of the simulation. This can even be seen for the flat field curve in the right panel of Fig. 10. The increased performance of the dark field parameter for larger FOVs is based on the reduced computation time required for each ray in the simulation. Hence, the resulting decrease in execution time also scales

-- Compressed PDF version --

Optics EXPRESS

quadratically with the FOV, and is already close to an order of magnitude for the 100×100 detector.

For the validity limit experiment, no signal deviations were found under the saturation point of the dark field signal. The dark field saturation presumably happens due to a breakdown of the IC model, i.e. the curve is broadened so much that it becomes almost impossible to differentiate between IC variance and offset. Therefore, we decided it was not meaningful to search for a condensed history model limit beyond this point where the IC model already partially broke down. Note that this is distinct from dark field saturation due to beam hardening, as was observed in the FleXCT data of the first experiment. In polychromatic acquisitions, both effects can occur simultaneously. The main experimental parameter of the experiment was the sample thickness. Hence, samples with a relatively simple geometry could be used. Additional simulation experiments with more complex sample geometries could be used for more detailed validation. However, we do not expect any problems on this front, as the only requirement of our model is the ray propagation distance through the mesh to be known. This distance is calculated during the ray tracing process, independent of the complexity of the geometry the ray is traversing through. To compare the IC curves in the right panel of Fig. 11, an attenuation correction was applied to the condensed history IC curve. Because the same attenuation coefficient was used for the explicit micro structure (where there is no attenuating material between the structures) and condensed history simulations (which uses a solid material mesh), the attenuation was overestimated in the latter. In other words, for the condensed history simulation, the void space between micro structures was not taken into account. Calculating the fill-factor of the micro structure wedge mesh was found to provide an accurate compensation factor for this effect.

Notably, for the EI-CT experiment, the explicit micro structure reconstructions contain a higher level of noise than their condensed history counterparts. This is likely due to the CAD-ASTRA simulation model, where a finite number of spatially distributed rays is used to sample an object and a small difference in ray position can lead to a very different trajectory through the micro structures, leading to a high variance signal from pixel to pixel. When looking at the box plots in Fig. 13, however, it is found that the underlying mean dark field signal within the different cylinders is accurately modeled using the condensed history model. Together with the simulation speed increase found in the previous experiments, the observed reduced noise content makes the condensed history model a prime candidate for performant and qualitative EI-CT simulations. Whenever the attenuation signal is also of interest, a compensation factor based on the micro structure fill-factor can be calculated to obtain quantitative results.

In the above experiments, the dark field is assumed to be isotropic. However, it is known that the shape and orientation of the micro structures can give the dark field signal a directional dependence (most notably in the case of fiber bundles). In this case, reconstruction of the dark field signal is known as dark field tensor tomography [36]. To incorporate the directional dependence in the condensed history dark field model, future work will involve upgrading the scalar dark field parameter to a tensor formulation. This way, the direction along which a ray travels through a dark field mesh will influence the actual dark field update applied when exiting the mesh.

It is important to point out that the proposed condensed history model is not exclusive to the EI setup or the CAD-ASTRA simulation toolbox. While EI was the XPCI setup considered in this work, our condensed history simulation model can also be applied in other XPCI setup simulations, such as analyzer-based imaging [14], as long as a ray optics model is a sufficiently accurate model to describe the setup. There also exist XPCI setups for which refraction has previously been accurately modeled using ray tracing, e.g. propagation-based imaging [15] and speckle imaging [9], but for which dark field simulations are thus far performed using wave optics [12,13]. The condensed history dark field method could also be applicable for these methods, but further research is required to validate this. Analogously, while CAD-ASTRA was used in

-- Compressed PDF version --

Optics EXPRESS

this work, any ray tracing based simulation framework can be extended to perform the proposed condensed history update during simulations.

6. Conclusion

In this work, we introduced a dark field material parameter in the CAD-ASTRA simulation toolkit. The dark field parameter is used in a condensed history approach to remove the need for explicit micro structures in the virtual sample models. Dark field parameters were successfully calibrated and then validated on real dark field data of different powders. It is found that our condensed history simulations provide a simulation speed increase that scales linearly with mesh thickness and quadratically with field of view, while still proving accurate results and even lower noise reconstructions in the case of EI-CT simulations. In future work, the dark field parameter can be expanded to a higher rank tensor to include directional dark field effects.

Funding. Fonds Wetenschappelijk Onderzoek (G094320N, G090020N), FoodPhase (S003421N), FWO-SB scholarship (1S46122N)).

Disclosures. The authors declare no conflicts of interest.

Data availability. Data and software code underlying the results presented in this paper may be obtained from the authors upon reasonable request.

References

1. K. Willer, A. Fingerle, W. Noichl, *et al.*, "X-ray dark-field chest imaging for detection and quantification of emphysema in patients with chronic obstructive pulmonary disease: a diagnostic accuracy study," Lancet Digital Health **3**(11), e733–e744 (2021).
2. F. Schwab, S. Schleede, D. Hahn, *et al.*, "Comparison of contrast-to-noise ratios of transmission and dark-field signal in grating-based x-ray imaging for healthy murine lung tissue," Z. Med. Phys. **23**(3), 236–242 (2013).
3. F. Gassert, T. Urban, M. Frank, *et al.*, "X-ray dark-field chest imaging: qualitative and quantitative results in healthy humans," Radiology **306**(2), e229037 (2023).
4. T. Partridge, A. Astolfo, S. S. Shankar, *et al.*, "Enhanced detection of threat materials by dark-field x-ray imaging combined with deep neural networks," Nat. Commun. **13**(1), 4651 (2022).
5. A. Astolfo, I. Haig, D. Bate, *et al.*, "Increased material differentiation through multi-contrast x-ray imaging: a preliminary evaluation of potential applications to the detection of threat materials," Phys. Scr. **98**(9), 095501 (2023).
6. L. Massimi, S. J. Clark, S. Marussi, *et al.*, "Dynamic multicontrast x-ray imaging method applied to additive manufacturing," Phys. Rev. Lett. **127**(21), 215503 (2021).
7. D. Shoukroun, L. Massimi, M. Endrizzi, *et al.*, "Edge illumination x-ray phase contrast imaging for impact damage detection in cfrp," Mater. Today Commun. **31**, 103279 (2022).
8. J. He, L. Van Doorselaer, A. Tempelaere, *et al.*, "Nondestructive internal disorders detection of 'Braeburn' apple fruit by X-ray dark-field imaging and machine learning," Phys. Med. Biol. **214**, 112981 (2024).
9. L. Quénot, E. Brun, J. M. Létang, *et al.*, "Evaluation of simulators for x-ray speckle-based phase contrast imaging," Phys. Med. Biol. **66**(17), 175027 (2021).
10. H. Wang, Y. Kashyap, and K. Sawhney, "From synchrotron radiation to lab source: advanced speckle-based X-ray imaging using abrasive paper," Sci. Rep. **6**(1), 20476 (2016).
11. P. R. T. Munro, "Rigorous multi-slice wave optical simulation of x-ray propagation in inhomogeneous space," J. Opt. Soc. Am. A **36**(7), 1197–1208 (2019).
12. M.-C. Zdora, P. Thibault, F. Pfeiffer, *et al.*, "Simulations of x-ray speckle-based dark-field and phase-contrast imaging with a polychromatic beam," J. Appl. Phys. **118**(11), 113105 (2015).
13. T. E. Gureyev, D. M. Paganin, B. Arhatari, *et al.*, "Dark-field signal extraction in propagation-based phase-contrast imaging," Phys. Med. Biol. **65**(21), 215029 (2020).
14. L. Rigon, F. Arfelli, and R.-H. Menk, "Three-image diffraction enhanced imaging algorithm to extract absorption, refraction, and ultrasmall-angle scattering," Appl. Phys. Lett. **90**(11), 114102 (2007).
15. J. Yan, J. Zheng, Z. Chen, *et al.*, "Monte carlo-based simulation of x-ray phase-contrast imaging for diagnosing cold fuel layer in cryogenic implosions," AIP Adv. **9**(2), 025311 (2019).
16. E. Pietersoone, J. M. Létang, S. Rit, *et al.*, "Combining wave and particle effects in the simulation of x-ray phase contrast–a review," Instruments **8**(1), 8 (2024).
17. J. P. Wilde and L. Hesselink, "Modeling of an x-ray grating-based imaging interferometer using ray tracing," Opt. Express **28**(17), 24657–24681 (2020).
18. A. Olivo, "Edge-illumination x-ray phase-contrast imaging," J. Phys.: Condens. Matter **33**(36), 363002 (2021).
19. P. R. Munro, K. Ignatyev, R. D. Speller, *et al.*, "The relationship between wave and geometrical optics models of coded aperture type x-ray phase contrast imaging systems," Opt. Express **18**(5), 4103–4117 (2010).

-- Compressed PDF version --

Optics EXPRESS

20. P. Paramonov, N. Francken, J. Renders, *et al.*, "CAD-ASTRA: a versatile and efficient mesh projector for X-ray tomography with the ASTRA-toolbox," Opt. Express **32**(3), 3425–3439 (2024).
21. L. Brombal, L. Rigon, F. Arfelli, *et al.*, "A Geant4 tool for edge-illumination X-ray phase-contrast imaging," J. Instrum. **17**(01), C01043 (2022).
22. J. Sanctorum, J. De Beenhouwer, and J. Sijbers, "X-ray phase contrast simulation for grating-based interferometry using GATE," Opt. Express **28**(22), 33390–33412 (2020).
23. T. P. Millard, M. Endrizzi, P. C. Diemoz, *et al.*, "Monte Carlo model of a polychromatic laboratory based edge illumination x-ray phase contrast system," Rev. Sci. Instrum. **85**(5), 053702 (2014).
24. K. Bhan and J. Spanier, "Condensed history Monte Carlo methods for photon transport problems," J. Comput. Phys. **225**(2), 1673–1694 (2007).
25. I. Kawrakow, "Accurate condensed history monte carlo simulation of electron transport. i. egsnrc, the new egs4 version," Med. Phys. **27**(3), 485–498 (2000).
26. T. A. Leatham, D. M. Paganin, and K. S. Morgan, "X-ray phase and dark-field computed tomography without optical elements," Opt. Express **32**(3), 4588–4602 (2024).
27. M. Bech, O. Bunk, T. Donath, *et al.*, "Quantitative x-ray dark-field computed tomography," Phys. Med. Biol. **55**(18), 5529–5539 (2010).
28. W. van Aarle, Willem Jan Palenstijn, J. Cant, *et al.*, "Fast and flexible X-ray tomography using the ASTRA toolbox," Opt. Express **24**(22), 25129–25147 (2016).
29. N. Francken, J. Sanctorum, J. Renders, *et al.*, "A condensed history approach to x-ray dark field effects in edge illumination phase contrast simulations," in *2023 45th Annual International Conference of the IEEE Engineering in Medicine & Biology Society (EMBC)*, (2023), pp.1–4.
30. M. Endrizzi and A. Olivo, "Absorption, refraction and scattering retrieval with an edge-illumination-based imaging setup," J. Phys. D: Appl. Phys. **47**(50), 505102 (2014).
31. M. Endrizzi, P. C. Diemoz, T. P. Millard, *et al.*, "Hard X-ray dark-field imaging with incoherent sample illumination," Appl. Phys. Lett. **104**(2), 024106 (2014).
32. N. Francken, J. Sanctorum, P. Paramonov, *et al.*, "Edge illumination x-ray phase contrast simulations using the CAD-ASTRA toolbox," Opt. Express **32**(6), 10005–10021 (2024).
33. B. De Samber, J. Renders, T. Elberfeld, *et al.*, "FleXCT: a flexible X-ray CT scanner with 10 degrees of freedom," Opt. Express **29**(3), 3438–3457 (2021).
34. B. Huyge, P.-J. Vanthienen, N. Six, *et al.*, "Adapting an XCT-scanner to enable edge illumination X-ray phase contrast imaging," e-Journal of Nondestructive Testing **28** (2023).
35. A. Doherty, S. Savvidis, C. Navarrete-León, *et al.*, "Edge-illumination x-ray dark-field tomography," Phys. Rev. Appl. **19**(5), 054042 (2023).
36. A. Malecki, G. Potdevin, T. Biernath, *et al.*, "X-ray tensor tomography(a)," Europhys. Lett. **105**(3), 38002 (2014).

146.102.254.11 2025-02-09 09:40:2